Journal Pre-proofs

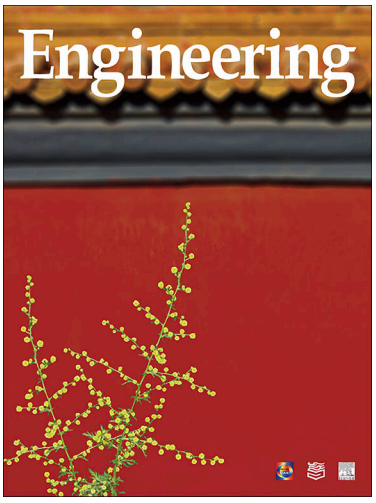

Article

Stabilization of Sub-Nanometer Pt Clusters on CoO_x Nano-Islands by Area-Selective Atomic Layer Deposition and Machine Learning Insights

Rongli Ye, Fangwen Ye, Junyang Chen, Xianbao Duan, Yaohui Dun, Bin Shan, Kun Cao, Rong Chen

PII: S2095-8099(25)00820-3
DOI: https://doi.org/10.1016/j.eng.2025.10.037
Reference: ENG 2206

To appear in: *Engineering*

Received Date: 29 May 2025
Revised Date: 30 September 2025
Accepted Date: 30 October 2025

Please cite this article as: R. Ye, F. Ye, J. Chen, X. Duan, Y. Dun, B. Shan, K. Cao, R. Chen, Stabilization of Sub-Nanometer Pt Clusters on CoO_x Nano-Islands by Area-Selective Atomic Layer Deposition and Machine Learning Insights, *Engineering* (2026), doi: https://doi.org/10.1016/j.eng.2025.10.037

This is a PDF of an article that has undergone enhancements after acceptance, such as the addition of a cover page and metadata, and formatting for readability. This version will undergo additional copyediting, typesetting and review before it is published in its final form. As such, this version is no longer the Accepted Manuscript, but it is not yet the definitive Version of Record; we are providing this early version to give early visibility of the article. Please note that Elsevier's sharing policy for the Published Journal Article applies to this version, see: https://www.elsevier.com/about/policies-and-standards/sharing#4-published-journal-article. Please also note that, during the production process, errors may be discovered which could affect the content, and all legal disclaimers that apply to the journal pertain.

© 2026 THE AUTHORS. Published by Elsevier LTD on behalf of Chinese Academy of Engineering and Higher Education Press Limited Company

Research

Frontiers of Extreme Manufacturing—Article

Stabilization of Sub-Nanometer Pt Clusters on CoO_x Nano-Islands by Area-Selective Atomic Layer Deposition and Machine Learning Insights

Rongli Ye [a], Fangwen Ye [b], Junyang Chen [c], Xianbao Duan [b], Yaohui Dun [c], Bin Shan [c], Kun Cao [a,*], Rong Chen [a,*]

[a] *State Key Laboratory of Intelligent Manufacturing Equipment and Technology, School of Mechanical Science and Engineering, Huazhong University of Science and Technology, Wuhan 430074, China*

[b] *Hubei Key Laboratory of Plasma Chemistry and Advanced Materials and School of Materials Science and Engineering, Wuhan Institute of Technology, Wuhan 430205, China*

[c] *State Key Laboratory of Material Processing and Die & Mould Technology, School of Materials Science and Engineering, Huazhong University of Science and Technology, Wuhan 430074, China*

[*] Corresponding authors.

Email addresses: kuncao@hust.edu.cn (K. Cao), rongchen@mail.hust.edu.cn (R. Chen)

Abstract: Sub-nanometer metallic clusters have attracted considerable interest owing to their high surface area and size-dependent properties. However, their high surface energies cause thermal instability, leading to aggregation and sintering that limit practical applications. In this study, we obtained sub-nanometer Pt clusters (average size ~0.76 nm) with highly stable configuration, deposited on CoO_x nano-islands by area-selective deposition (ASD). The Pt-CoO_x structures exhibited low Pt loading and high deposition selectivity. During ASD, Pt clusters were selectively deposited on CoO_x regions, where strong metal-support interactions (MSI) between Pt and CoO_x supported effective anchoring. Subsequent H_2 post-treatment promoted electron transfer between Pt and CoO_x as well as Pt cluster migration from the Al_2O_3 substrate to the CoO_x nano-islands, particularly at the Al_2O_3-CoO_x interface, further improving selectivity. Potential simulations by machine learning revealed directional Pt migration and provided atomic-level insights into stabilization mechanisms. After high-temperature (at 600 °C) aging, Pt clusters remained highly dispersed without noticeable sintering, owing to the synergistic effects of physical isolation by CoO_x nano-islands and strong MSI. This synergistic strategy holds practical relevance for industrial applications and provides a robust framework for designing durable catalytic structures.

Keywords: Sub-nanometer Pt clusters; Thermal stability; Area-selective deposition; Interfacial interaction; Machine learning potential

1. Introduction

Ultrasmall metallic nanoclusters have unique advantages in energy, catalysis, and environmental applications because of their exceptional properties [1–5]. However, the high surface energy of metallic nanoclusters renders them susceptible to migration and agglomeration during catalytic reactions, leading to particle size enlargement as a mechanism for minimizing the system energy [6–8]. This sintering process not only results in the loss of noble metals but also alters the surface-active sites and electronic properties, thereby causing irreversible deactivation and substantial degradation in catalytic performance. Therefore, it is essential to elucidate the stabilization mechanisms of metallic nanoclusters and develop highly stable sintering-resistant configurations to ensure their long-term performance under harsh conditions.

Journal Pre-proofs

Several stabilization strategies have been developed to suppress nanocluster sintering. However, challenges persist, particularly for sub-nanometer metallic clusters. These strategies can be broadly classified into the following categories: physical confinement by coating or encapsulation of nanoclusters or utilization of metal-support interactions (MSI) to anchor them. However, such approaches demand fabrication accuracy at the atomic level owing to the inherent trade-off between surface atom utilization and thermal stability [9–14]. Among various fabrication approaches, atomic layer deposition (ALD) has been employed for atomic-level structural preparation due to its precise thickness, composition control, and excellent conformality [15–18]. Fabrication of physical confinement structures by ALD is an effective approach towards suppressing the migration and aggregation of metal nanoparticles by introducing spatial barriers. For example, the deposition of ZrO_2 nanocages around Pt/C catalysts via ALD has been shown to generate open yet confining architectures in polymer electrolyte fuel cells (PEFCs), significantly improving their stability under electrochemical conditions [19]. Similarly, encapsulating Pt nanoparticles within an Al_2O_3 framework has proven effective in preventing sintering in the presence of oxygen or steam, while maintaining small particle sizes in Pd–Pt bimetallic systems [20]. In another study, facet-selective ALD of CeO_x on Pt nanoparticles was developed to encapsulate Pt with specific facets and expose active sites, resulting in remarkable stability and improved catalytic activity [21].

Enhancing MSI is another strategy adopted to anchor metal nanoparticles and inhibit their mobility. For instance, constructing embedded nano-trap structures via CoO_x ALD around Pt nanoparticles establishes strong MSI, thereby effectively immobilizing the nanoparticles, while preserving accessible active sites [22]. Moreover, recent studies have highlighted that optimal MSI strength is critical for stability; excessively strong MSI may block active sites and hinder catalytic activity, whereas insufficient MSI cannot effectively suppress sintering. Therefore, the design of interfacial structures with balanced MSI strength has emerged as a key principle [19,23–26]. A synergistic approach that combines physical confinement and MSI has shown great promise for achieving both stability and catalytic performance. Integrated structures that simultaneously restrict nanoparticle migration and enhance anchoring strength have demonstrated superior resistance to sintering under high temperature and redox conditions. CeO_x exhibits stronger affinity than SiO_2 for Au nanoparticles, enabling the formation of a stronger MSI that effectively anchors the Au nanoparticles. In contrast, the weaker interaction between Au and SiO_2 has been reported to cause significant sintering of the anchored nanoparticles [27].

In this study, CoO_x nano-islands with highly stable configuration anchored on sub-nanometer Pt clusters with low noble metal loading was prepared by area-selective deposition (ASD). Density functional theory (DFT) calculations indicated that the Pt precursors preferentially adsorbed on CoO_x rather than on the Al_2O_3 substrate. By fine-tuning the ALD deposition temperature, pulse times, and co-reactants, selective deposition was achieved, yielding Pt deposition exclusively on the CoO_x nano-island area with a selectivity of up to 95.1%. Post-treatment in H_2 further enhanced selectivity by promoting Pt migration from the non-growth area of Al_2O_3 substrate to the growth area of CoO_x nano-islands, facilitating electron transfer between Pt and Co, and strengthening MSI. The isolation effect and interfacial interaction of CoO_x nano-islands as stabilizers enabled the Pt clusters to withstand high-temperature aging under oxidative and reductive conditions.

2. Materials and methods

2.1. Synthesis of Pt/CoO_x/Al_2O_3 catalysts

Al_2O_3 powder was selected as the support and dried in a muffle furnace at 900 °C for 24 h [22]. Subsequently, 1 g of the support was added to 50 mL of deionized water and stirred for 20 min, after which the support was fully dispersed by ultrasonication for 1 h. Next, 0.05 g of $Co(NO_3)_2{\cdot}6H_2O$ was added to the solution and stirred for 20 min. The pH of the solution was adjusted to 9 using a 0.5 mol·L^{-1} Na_2CO_3 aqueous solution and stirred for 2 h at room temperature. The stock solution was centrifuged at 3500 r·min^{-1}, washed with deionized water and anhydrous ethanol three times, respectively, and then placed in a vacuum drying oven at 100 °C for overnight drying. The dried powder was placed in a tube furnace and calcined at 400 °C for 4 h at a ramp rate of 2 °C·min^{-1} [28]. The resulting sample is denoted as CoO_x/Al_2O_3.

For each Pt ALD process, approximately 100 mg of the support was loaded into a custom-made fluidized ALD reactor. The $MeCpPtMe_3$ precursor was maintained at 65 °C, and the pulse pressure was set to 0.15 Torr (1 Torr = 1.33 × 10^2 Pa). Before each deposition, the powder was activated with O_2 for 10 min to provide more reaction sites. The flow rate of the O_2 precursor was 500 mL·min^{-1}. The resulting samples are denoted as Pt/CoO_x/Al_2O_3. The Pt-loaded Al_2O_3 and CoO_x single supports are denoted

as Pt/Al_2O_3 and Pt/CoO_x, respectively. To investigate the thermal stability of the prepared catalysts, the samples were subjected to aging treatment. Unless otherwise specified, aging was conducted at 600 ℃ for 4 h in an atmosphere of 21% O_2/N_2.

2.2. Definition of selectivity

ASD is an ALD-based deposition method in which a target material is deposited with controlled thickness onto designated growth areas composed of either the same or different material systems. In contrast, little or no deposition occurs on non-growth areas. The difference in chemical reactivity between the growth and non-growth areas is defined as selectivity, which is typically quantified using the following formula:

$$\text{Selectivity} = \frac{\theta_{GA} - \theta_{NGA}}{\theta_{GA} + \theta_{NGA}} \quad (1)$$

Where θ_{GA} and θ_{NGA} represent the amounts of material present after deposition on the growth and non-growth areas, respectively [29,30]. Similarly, the selectivity of Pt on a powder substrate is defined as:

$$\text{Selectivity} = \frac{wt_1 - wt_2}{wt_1 + wt_2} \quad (2)$$

where wt_1 refers to the Pt loading deposited on the growth region (CoO_x) using the ALD process, and wt_2 denotes the Pt loading on the non-growth region (Al_2O_3) under the same ALD conditions. Therefore, the selectivity was calculated based on wt_1 and wt_2, both obtained using identical ALD parameters.

2.3. Characterization of $Pt/CoO_x/Al_2O_3$ catalysts

The Pt content deposited on the CoO_x/Al_2O_3 support using inductively coupled plasma optical emission spectrometer (ICP-OES) was used on an AvioTM 200 Max (PerkinElmer, USA). Before the test, samples were kept immersed in aqua regia overnight, and deionized water was added to reduce the acidity of the solution to < 5%.

Raman spectra of fresh and aged catalysts were recorded using a Raman spectrometer (LabRAM HR800) (Renishaw, UK) equipped with a 532 nm Ar-ion laser to investigate the phases and vibrational modes in CoO_x. X-ray diffraction (XRD) was performed at 40 kV and 40 mA using Cu Kα radiation (λ = 1.5406 Å) on MAXima_X XRD-7000 instrument (Shimadzu Corporation, Japan) to characterize the phase structure of fresh and aged catalysts. Diffuse-reflectance infrared Fourier-transform spectroscopy (DRIFTS) was conducted using a Fourier-transform infrared (FTIR) spectrometer (Nicolet iS50, Thermo Fisher Scientific, USA) equipped with a wide-band mercury–cadmium–telluride (MCT-A) detector (Thermo Fisher Scientific) and a Harrick high-temperature cell (Thermo Fisher Scientific) to investigate different CO adsorption species on Pt using fresh and aged catalysts. The samples were gradually heated to 300 °C and held for 30 min to minimize the influence of moisture and CO_2 in the air on the IR spectroscopic measurements. The temperature was then lowered to 30 ℃ for the spectral acquisition. Background spectrum was first collected under an Ar atmosphere, followed by CO for adsorption measurements. Finally, the gas was switched to Ar to purge the surface via physical adsorption. X-ray photoelectron spectroscopy (XPS) was performed using a Thermo Scientific K-Alpha instrument (Thermo Fisher Scientific) with Al Kα radiation. Charge correction for both the survey and high-resolution spectra was based on the C 1s peak of contaminated carbon at 284.8 eV. Morphology and structural analyses were conducted by transmission electron microscopy (TEM) (Thermo Fisher Scientific), high-angle annular dark-field–scanning transmission electron microscopy (HAADF-STEM; Thermo Fisher Scientific), and energy-dispersive X-ray spectroscopy (EDS; Thermo Fisher Scientific) mapping on a Thermo Fisher Talos F200s instrument (Thermo Fisher Scientific) operated at 200 kV.

3. Theoretical calculation and simulation

All the energy calculations in this study were performed within the DFT framework using the Vienna Ab initio Simulation Package (VASP). The exchange-correlation energy was treated within the framework of the generalized gradient approximation (GGA), specifically employing the Perdew–Burke–Ernzerhof (PBE) functional. To ensure sufficient electronic convergence, the

energy and force convergence criteria were set at 1×10^{-5} eV and 0.02 eV/Å, respectively. Geometric optimizations were performed using the conjugate gradient (CG) algorithm, allowing full relaxation of both the atomic positions and lattice parameters. A plane-wave cutoff energy of 400 eV was used to balance computational accuracy and efficiency. To account for weak interactions involved in molecular adsorption processes, van der Waals forces were incorporated using the Grimme DFT-D3 (BJ) dispersion correction scheme (Integer parameter for Van der Waals correction method, IVDW = 12, IVDW: integer parameter for Van der Waals correction method).

To accurately evaluate the adsorption behavior of the precursor trimethyl(methylcyclopentadienyl)platinum ($MeCpPtMe_3$) on different support surfaces, a standard molecular structure (mol format) of $MeCpPtMe_3$ was obtained from authoritative databases, such as ChemicalBook. The molecular geometry was fully optimized in vacuum to determine the most stable ground-state configuration. Subsequently, the optimized precursor structure was adsorbed onto the Al_2O_3 (001) and Co_3O_4 (110) surfaces to construct complex adsorption systems. The entire model was then geometrically optimized with all atomic positions fully relaxed, while the substrate lattice constants were fixed.

To prevent artificial interactions arising from periodic boundary conditions, a 20 Å vacuum layer was introduced along the *z*-direction of the adsorption models. The adsorption energy was calculated using the following equation:

$$E_{ads} = E_{MeCpPtMe_3@surface} - E_{surface\ relaxed} - E_{MeCpPtMe_3\ relaxed} \quad (1)$$

Where $E_{MeCpPtMe_3@surface}$ represents the total energy of the optimized adsorption structure, $E_{surface\ relaxed}$ represents the energy of the isolated support surface, and $E_{MeCpPtMe_3\ relaxed}$ represents the energy of the gas-phase optimized precursor. This methodology systematically accounts for molecular configuration relaxation, charge redistribution, and weak interactions, thereby improving the accuracy of adsorption energy calculations and enabling reliable comparisons between different systems. The established protocol reveals intrinsic differences in precursor adsorption strength on various support surfaces, providing crucial theoretical support for the subsequent analysis of strong MSI effects and interface regulation.

Based on the developed machine-learning potential (MLP) for the Al_2O_3-Co_3O_4-Pt ternary system, large-scale molecular dynamics (MD) simulations were conducted to investigate the migration behavior of Pt nanoparticles across different support interfaces and to elucidate the associated sintering dynamics. In the MD model, an Al_2O_3 (001) surface was used as the primary support, onto which Co_3O_4 island structures of varying sizes were constructed to mimic the distribution of localized functional regions in practical catalysts. Multiple Pt nanoparticles were randomly distributed between the Al_2O_3 substrate and Co_3O_4 islands, reflecting realistic variations in particle size and spatial arrangement. The simulation cell dimensions were set to 133 Å × 115 Å × 25 Å, comprising a total of 12 613 atoms. During the simulation, the system was uniformly heated from 300 to 900 K over a period of 10 ps, followed by a 15 ps isothermal run at 900 K. The results revealed pronounced migration of the Pt particles toward the Co_3O_4 islands, indicating a spontaneous anchoring mechanism driven by strong interfacial interactions. These findings provide kinetic insights into the sintering resistance imparted by composite support structures.

4. Results and discussions

Fig. 1(a) illustrates the synthesis of sub-nanometer Pt clusters anchored on CoO_x nano-islands, achieved via a two-step process. First, CoO_x nano-islands were fabricated on Al_2O_3 powder support using a deposition-precipitation method. Subsequently, the ASD technique was employed to selectively deposit Pt clusters, predominantly on the CoO_x nano-islands rather than on Al_2O_3, yielding the Pt/CoO_x/Al_2O_3 sample. The stabilization of Pt clusters after H_2 treatment can be attributed to three main mechanisms: ① migration of Pt clusters from the Al_2O_3 support to CoO_x nano-islands, promoting stronger anchoring via MSI between Pt and CoO_x; ② reduction of PtO_x, which is prone to sintering; and ③ isolation of Pt on CoO_x, further improving Pt cluster stability. Figs. 1(b) and (c) present the TEM images of Pt/CoO_x/Al_2O_3, where the Pt and CoO_x mixed clusters, indicated by white dotted circles, can be observed to be uniformly dispersed on the support. The EDS elemental mapping of the Pt/CoO_x/Al_2O_3 sample (Fig. S1 in Appendix A) further confirms this high dispersion, with no significant Pt aggregation detected. Additionally, the estimated lattice spacings of 0.46 and 0.23 nm correspond to the (111) and (222) crystal facets of Co_3O_4, respectively.

Raman spectroscopy and XRD analyses were performed to characterize the crystal structures of the components. As shown in Fig. 1(d), CoO_x exhibited vibrational modes at 480, 521, 617, and 688 cm^{-1}, corresponding to the E_g, F_{2g}, F_{2g}, and A_{1g} modes, respectively, confirming the presence of Co_3O_4 [31–33]. This is consistent with the crystal structure observed in the XRD pattern (Fig. S2 in Appendix A). In contrast, Al_2O_3 exhibited no Raman activity. Upon Pt deposition, the vibrational peaks of CoO_x weakened significantly, suggesting the selective deposition of Pt onto CoO_x. Fig. 1(e) shows the XRD patterns of the samples, where only the diffraction peak corresponding to Al_2O_3 was observed in the $Pt/CoO_x/Al_2O_3$ sample, with no distinct diffraction peaks for Pt or CoO_x were detected, likely because of their small mixed cluster sizes. Notably, after Pt deposition on CoO_x, the XRD peaks shifted to higher angles. According to Bragg's law, an increase in the diffraction angle (θ) corresponds to a decrease in the interplanar spacing (d), suggesting that the interaction between Pt and CoO_x induces lattice compression in CoO_x. In contrast, no such peak shift was observed for Pt/Al_2O_3, further supporting the stronger interaction between Pt and CoO_x than that between Pt and Al_2O_3.

The surface chemical valence states of Pt and Co were characterized using XPS, and the results are shown in Fig. 1(f). Owing to the overlap between Al 2p and Pt 4f orbitals caused by the Al_2O_3 support, the Pt 4d orbital was analyzed [34]. The XPS spectra revealed Pt^0 $4d_{5/2}$, Pt^{2+} $4d_{5/2}$, and Pt^{4+} $4d_{5/2}$ signals at 313.4, 316.0, and 317.9 eV, respectively. The combined content of Pt^{2+} and Pt^{4+} accounted for 87.19%, with the remaining fraction corresponding to Pt^0, indicating that Pt predominantly exists in an oxidized state with minimal metallic content. Such a high oxidation state may compromise the stability of Pt clusters, making them more prone to sintering. For the Co 2p orbital, binding energies corresponding to the Co^{3+} $2p_{3/2}$, Co^{2+} $2p_{3/2}$, and satellite peaks are observed at 780.8, 782.6, and 787.4 eV, respectively [35,36]. XPS confirmed that CoO_x exists as Co_3O_4, with a theoretical Co^{2+}/Co^{3+} ratio was 0.5. However, in the $Pt/CoO_x/Al_2O_3$ sample, the observed Co^{2+}/Co^{3+} ratio increased to approximately 1.3, which may be attributed to the interaction between Pt and CoO_x. This interaction possibly leads an increase in the high-valence Pt content while simultaneously reducing the proportion of high-valence Co species.

To further investigate the local bonding environment of Pt, DRIFTS experiments were conducted using CO adsorption, owing to its high sensitivity. As shown in Fig. S3 (in Appendix A), CO absorption produced four peaks at 2173, 2106, 2089, 2069, and 1840 cm^{-1}, corresponding to CO adsorption on PtO_x (CO–PtO_x), well-coordinated Pt sites (CO–Pt_{WC}), under-coordinated Pt sites (CO–Pt_{LC}), and bridge sites (CO–Pt_{NP}), respectively [37,38]. The detection of PtO_x-related signals confirmed the oxidized state of Pt. To exclude the contribution of physical adsorption, Ar purging was performed, effectively removing the gas-phase CO peak at 2173 cm^{-1} [39,40].

Journal Pre-proofs

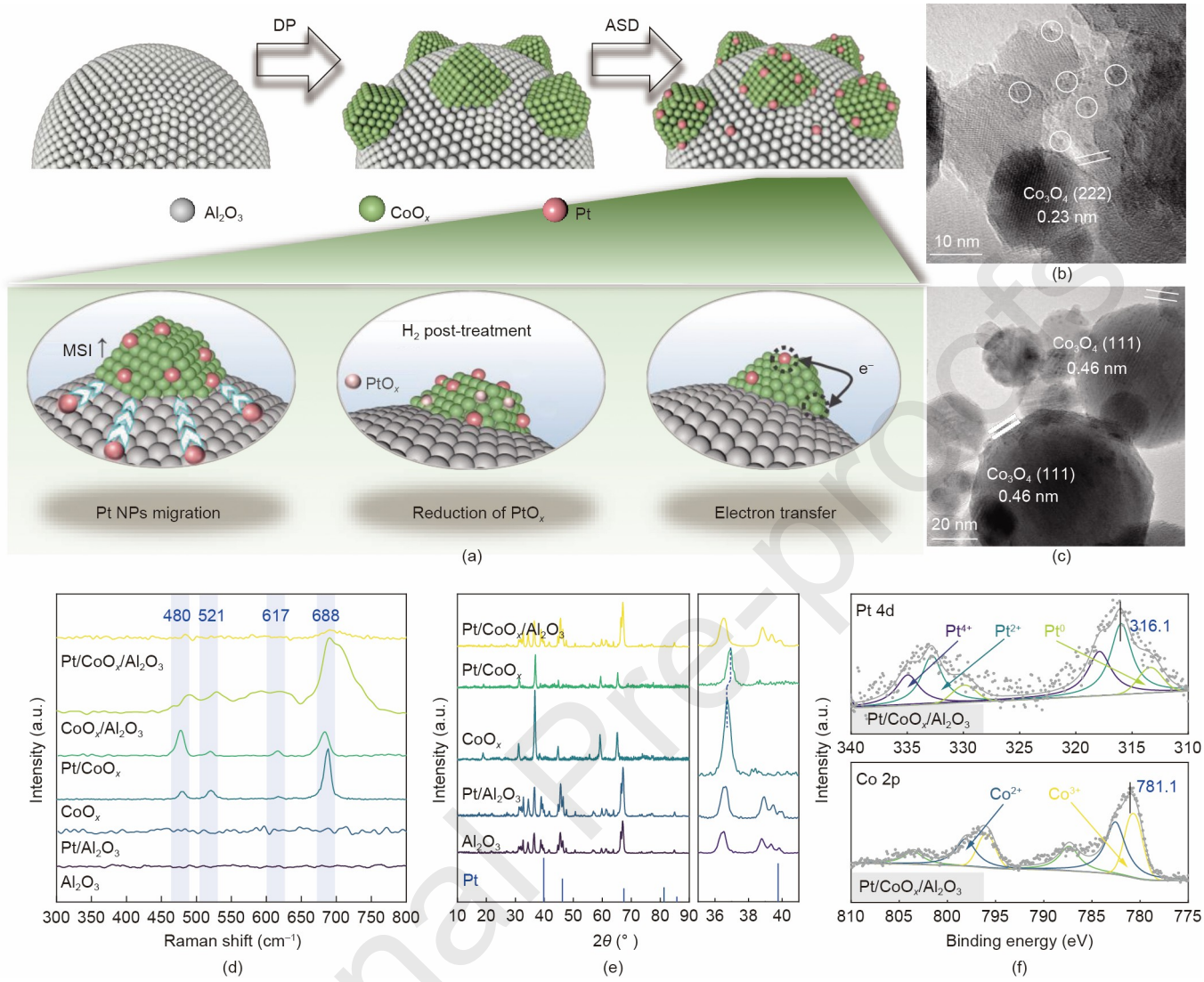

Fig. 1. (a) Schematic illustration of the synthesis process and stabilization mechanism of the $Pt/CoO_x/Al_2O_3$ catalyst; (b, c) TEM images of $Pt/CoO_x/Al_2O_3$ (Pt and CoO_x mixed clusters are marked with white dotted circles); (d) Raman spectra of Al_2O_3, Pt/Al_2O_3, CoO_x, Pt/CoO_x, CoO_x/Al_2O_3, and $Pt/CoO_x/Al_2O_3$ samples; (e) XRD patterns of Pt, Al_2O_3, CoO_x, Pt/Al_2O_3, Pt/CoO_x and $Pt/CoO_x/Al_2O_3$; (f) XPS spectra of Co 2p and Pt 4d orbitals of $Pt/CoO_x/Al_2O_3$.

As shown in Fig. 2(a), ALD facilitated the homogeneous dispersion of Pt clusters onto the Al_2O_3 support. However, after aging in an oxidizing atmosphere, the weak interaction between Pt and Al_2O_3 resulted in significant sintering, with particle size increasing from 0.76 to 10.28 nm, thereby reducing the overall surface area of the Pt clusters. In contrast, Fig. 2(b) shows that Pt nanoparticles on the CoO_x support exhibited less pronounced sintering owing to the stronger MSI. However, the relatively large initial size of CoO_x particles (7.61 nm) hindered the effective utilization of the Pt nanoparticles. The dispersion of Pt on CoO_x was significantly inferior to that on Al_2O_3. To overcome these limitations, a CoO_x nano-island-anchored sub-nanometer Pt cluster configuration was designed, combining the superior dispersion capability of Al_2O_3 with the strong anchoring ability of CoO_x. The morphology and particle size distribution of this configuration are shown in Fig. 2(c), with an average Pt cluster size of (0.76 ± 0.32) nm. To develop a highly accurate MLP, a comprehensive and representative training dataset was generated through systematic data acquisition and validation. T-SNE visualization (Fig. S4 in Appendix A) confirmed that the constructed dataset

fully covered the configurational space of the system, ensuring both representativeness and uniform distribution of training samples. The resulting Deep Potential Molecular Dynamics (DeepMD) based MLP demonstrated excellent performance in describing the Pt-Co_3O_4@Al_2O_3 ternary system with first-principles-level accuracy. Adsorption energies of a single Pt atom at various sites on Al_2O_3 and Co_3O_4 surfaces were calculated using both first-principles methods and the DeepMD machine learning potential. The two methods yielded consistent trends in relative adsorption energies, indicating that the constructed potential function achieves accuracy comparable to that of the first-principles calculations. Therefore, the framework used in this study can be considered suitable for simulating migration and sintering behaviors of Pt clusters (Table S1 in Appendix A). Furthermore, DFT-calculated adsorption energies of the $MeCpPtMe_3$ precursor on the Al_2O_3 and Co_3O_4 supports were –0.06 and –0.52 eV, respectively. These results indicate that the Pt precursor adsorbs more readily on Co_3O_4 than on Al_2O_3, owing to the ability of Co_3O_4 to dissociate oxygen and generate active sites for Pt deposition.

To enhance the selective deposition of Pt on the CoO_x regions, optimization of the ALD parameters is necessary. Typically, Pt-based ALD processes operate at temperatures ranging from 200 to 300 °C or utilize more oxidizing co-reactants, such as ozone or oxygen plasma, to accelerate the reaction rate [41–46]. However, at lower temperatures (e.g., 100 °C), although the precursor can adsorb on the surface, the adsorption and dissociation of molecular oxygen into atomic oxygen is hindered, thereby suppressing ligand combustion [47]. To reduce Pt adsorption and deposition on the Al_2O_3 support, the conventional saturation process (200-200-200-200) was replaced with a short-pulse, multicycle sequence, incorporating multiple short-pulse cycles (Fig. 2(d)). O_2 was selected as the co-reactant instead of O_3 because of its relatively weaker oxidizing properties and lower deposition temperature. Fig. 2(e) presents the Pt loadings on both substrates under different conditions, and Fig. 2(f) illustrates the corresponding selectivity values. At a deposition temperature of 150 °C, the selectivity for precursor pulses of 25, 100, and 200 s were 87.8%, 70.7%, and 87.9%, respectively. However, when the temperature was further reduced to 130 °C, the selectivity significantly decreased to 76.3%. Pretreatment of the support with hydrogen and oxygen improved the selectivity to 90.4% and 91.6%, respectively. The highest selectivity (95.1%) was achieved at 150 °C using a 50-50-50-50 pulse sequence over four cycles. Therefore, this condition was identified as the optimal ALD process for achieving the desired configuration of Pt on CoO_x nano-islands.

Journal Pre-proofs

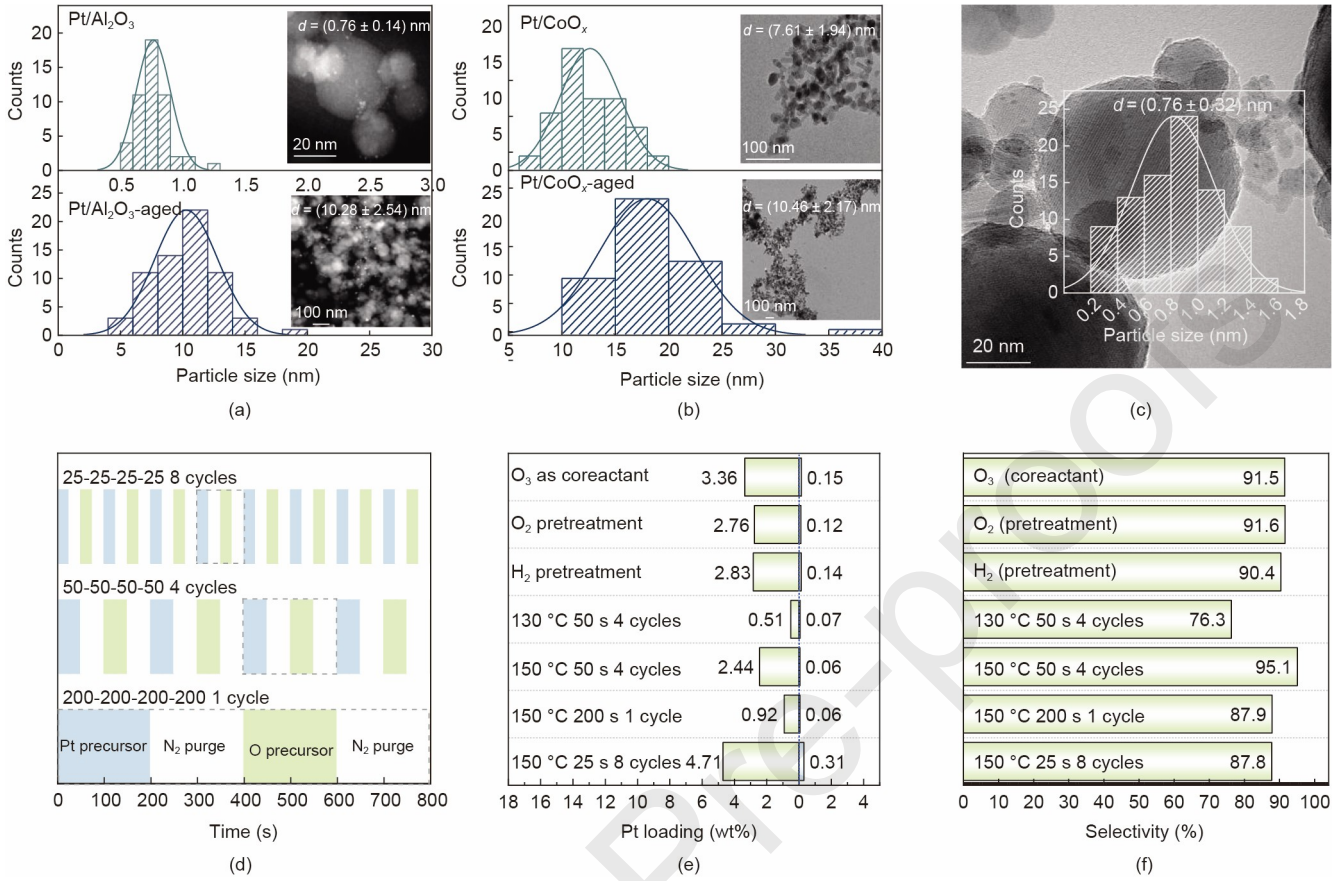

Fig. 2. Particle size distributions of: (a) Pt/Al_2O_3 and Pt/Al_2O_3-aged; (b) Pt/CoO_x and Pt/CoO_x-aged samples; (c) TEM image with the corresponding particle size distribution of $Pt/CoO_x/Al_2O_3$; (d) schematic diagram of the short pulse and multi-cycle process; (e) Pt loadings on Al_2O_3 and CoO_x supports obtained under different processes; (f) calculated selectivities corresponding to Pt loadings achieved by different ALD processes.

The stability of the Pt clusters in this configuration depends on two key factors: ① the anchoring effect of CoO_x on Pt and ② the reduction or elimination of PtO_x species, which are prone to sintering. To address the challenge of achieving high selectivity in ASD, studies have introduced temperature-controlled atmospheric treatments. In particular, the reducing effect of H_2 on PtO_x species further contributes to cluster stabilization. Therefore, the effects of temperature and atmosphere on Pt stability were systematically investigated. For the DRIFTS measurements, the samples were subjected to in situ heat treatment under oxidizing (O_2), inert (Ar), and reducing (H_2) atmospheres. Under an O_2 atmosphere (Fig. S5 in Appendix A), adsorption peaks at 2106 and 2090 cm^{-1} dominated, with no detectable bridge-site adsorption. Increasing the temperature caused the 2106 cm^{-1} peak to gradually shift to higher wavenumbers, indicating progressive oxidation of the Pt. Under an Ar atmosphere (Fig. S6 in Appendix A), CO adsorption peaks appeared at 2108, 2086, and 2077 cm^{-1}. With increasing temperature, the 2108 cm^{-1} peak exhibited a blueshift, similar to that observed under an O_2 atmosphere. Simultaneously, the bridge-site adsorption peak at 1842 cm^{-1} gradually weakened, suggesting potential Pt cluster aggregation. In contrast, under H_2 atmosphere (Fig. 3(a)), distinct adsorption peaks at 2109, 2083, 2062, and 1842 cm^{-1} were observed at 300 °C. With increasing temperature, the peak at 2109 cm^{-1} diminished while the other peaks remained. This behavior indicates that, under O_2 and Ar, the peaks above 2100 cm^{-1} correspond to CO adsorption on PtO_x, which promoted Pt sintering. However, in H_2 atmosphere, the disappearance of PtO_x can be attributed to its reduction, thereby enhancing Pt stability.

Annealing treatments were conducted in a tube furnace at 200, 400, and 600 °C (Fig. S7 in Appendix A). Under O_2 and N_2 atmospheres, PtO_x species persisted at temperatures below 400 °C. However, at 600 °C, the CO adsorption peaks at 2086 and

2063 cm^{-1}, corresponding to high- and low-coordinated Pt sites, respectively, exhibited a significant reduced, indicating increased atomic aggregation of Pt clusters. In contrast, H_2 treatment at 600 °C nearly eliminated CO adsorption on PtO_x species while adsorption on the two low-coordination Pt sites was largely preserved. These findings suggest that H_2 treatment at 600 °C enhances the interaction between Pt and CoO_x, thereby improving the stability of Pt clusters.

To further explore conditions that enhance MSI, the effects of H_2 pre- and post-treatment at different temperatures were investigated. Pre-treatment refers to H_2 treatment before Pt ALD, whereas post-treatment (or no special annotation) refers to H_2 treatment after Pt ALD. Figs. 3(b) and (c) show the results of CO DRIFTS and XRD characterizations of the samples. No distinct Pt diffraction peaks were observed, consistent with the small size of the Pt nanoclusters. For the samples post-treated at 600 °C, the PtO_x signals were significantly weakened, and the peaks associated with high-coordination Pt sites shifted to lower wavenumbers, indicating smaller Pt particle size and indicating reduced PtO_x coverage compared with those obtained after other treatments [48].

XPS analysis of the post-treatment sample revealed electron interactions between the Co 2p and Pt 4d orbitals (Figs. 3 (d) and (e)). The Pt 4d and Co 2p orbitals, in the sample post-treated at 600 °C, exhibited noticeable shifts in binding energy compared to those in the untreated $Pt/CoO_x/Al_2O_3$ sample. The Pt 4d orbital shifted from 316.1 to 315.6 eV and Co 2p orbital shifted from 781.1 to 781.7 eV, indicating enhanced electron transfer between Pt and CoO_x. Survey scans and O 1s spectra (Fig. 3(f) and Figs. S8 and S9 in Appendix A) further showed that after H_2 treatment, the O 1s peak from the Pt-deposited CoO_x/Al_2O_3 sample shifted to higher binding energy, confirming strong interaction between Pt and CoO_x during deposition. These results also demonstrate the selective deposition of Pt on CoO_x [49].

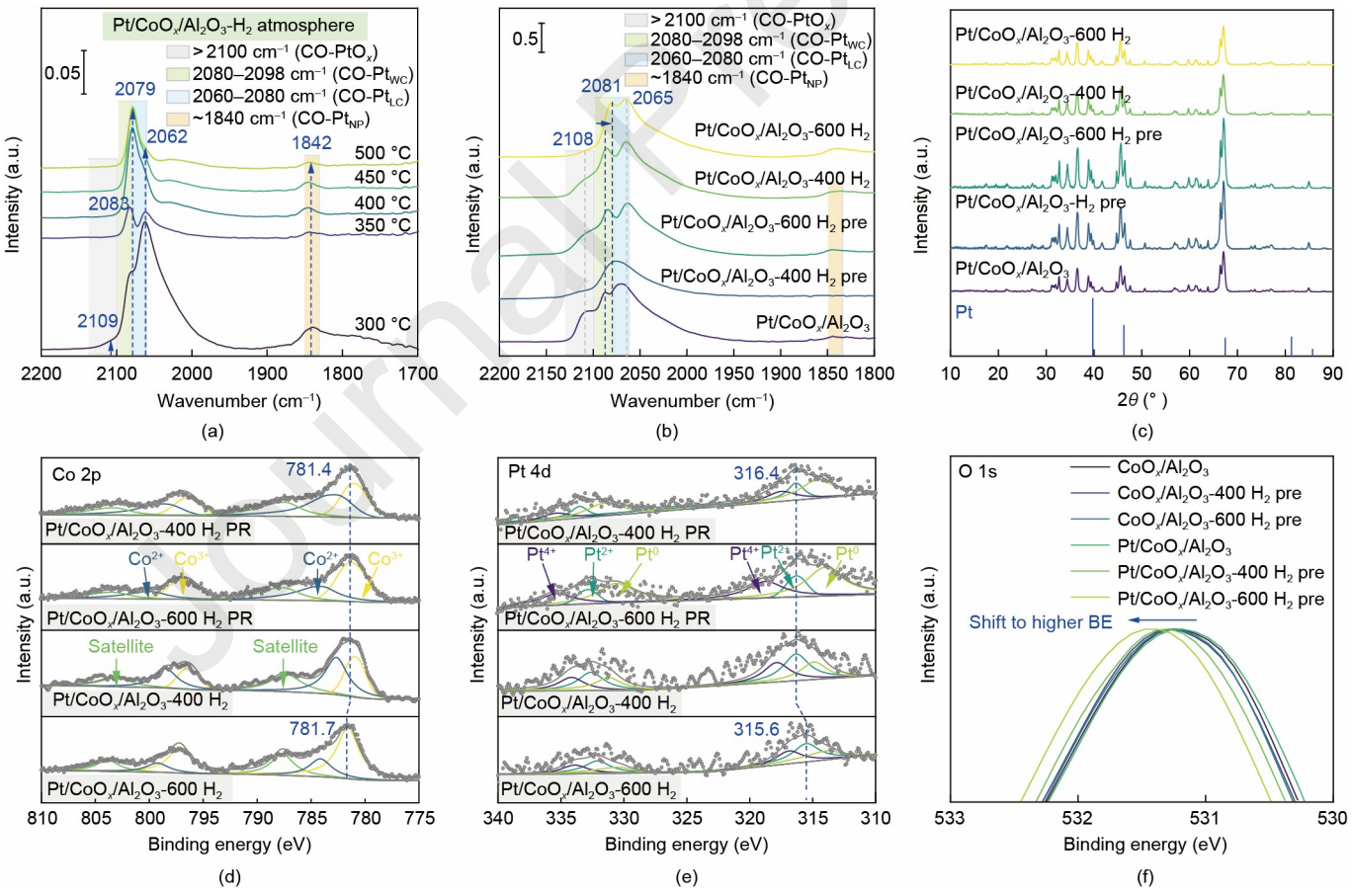

Fig. 3. (a) *In situ* CO DRIFTS spectra of $Pt/CoO_x/Al_2O_3$ in an H_2 atmosphere. Characterization of $Pt/CoO_x/Al_2O_3$ pre- and post-treated with H_2; (b) CO DRIFTS spectra, (c) XPD patterns, and XPS spectra of (d) Co 2p; (e) Pt 4d; and (f) O 1s orbitals.

Fig. S10 in Appendix presents the EDS elemental mapping and TEM images of the $Pt/CoO_x/Al_2O_3$ sample after H_2 post-treatment at 600 °C. No aggregation of the Pt nanoclusters was observed, indicating that the Pt nanoclusters remained well-dispersed and retained their size. The bright regions in the TEM images correspond to CoO_x clusters, consistent with the elemental mapping results. Compared with the untreated sample (Figs. S1(g) and (h)), the Pt and Co distributions in the post-treated sample were more concentrated, indicating enhanced Pt deposition selectivity on CoO_x, which contributed to improved thermal stability. Furthermore, lattice fringes with a spacing of 0.21 nm, corresponding to the Co-Pt (101) crystal facet (Fig. S11 in Appendix), indicate that H_2 post-treatment facilitates partial formation of Co-Pt alloy. To evaluate high-temperature stability of the H_2 treated samples, aging tests were conducted under oxidative conditions at elevated temperatures. XRD analysis (Fig. 4(a)) revealed no noticeable changes at 600 °C, indicating non-severe sintering under both oxidative and reductive conditions. When the aging temperature increased to 800 °C, diffraction peaks corresponding to Pt (111) and (222) crystal facets appeared, indicating sintering at this temperature. This observation is consistent with the CO adsorption data (Fig. 4(b)), signals corresponding to CO adsorption from the 800 °C-aged sample were nearly absent.

The wavenumber statistics of CO adsorption peaks at different Pt sites for the different samples are summarized in Table S2 in Appendix A. DRIFTS analysis further revealed that the H_2 pre-treated sample exhibited a CO adsorption peak above 2100 cm^{-1}, whereas the H_2 post-treated sample exhibited a CO adsorption peaks at lower wavenumbers. This shift suggests that Pt nanoclusters in the post-treated sample consisted of fewer atoms, indicating that H_2 post-treatment enhanced Pt cluster stability, likely due to stronger interaction between Pt and CoO_x, as previously discussed. For the H_2-post-treated sample, CO adsorption peaks were observed at both high- and low-coordination Pt sites at 600 °C, indicating that the number of surface Pt atoms remained relatively low. This result further confirms that H_2 post-treatment 600 °C effectively stabilizes Pt clusters, consistent with the enhanced electron transfer between Pt and CoO_x (Figs. 3(d) and (e)). Although the directly-aged $Pt/CoO_x/Al_2O_3$ sample retained the CO adsorption peaks at both high- and low-coordination sites, the presence of PtO_x species before and after aging may have facilitated sintering, rendering the Pt clusters more susceptible to aggregation. XPS analysis of Pt 4d and Co 2p orbitals, along with the corresponding proportions of Pt oxidation states for the aged $Pt/CoO_x/Al_2O_3$-600 H_2-aged sample, are shown in Figs. 4(c) and (d) and Table S3 in Appendix A. Compared with the directly-aged $Pt/CoO_x/Al_2O_3$ sample, the proportion of metallic Pt^0 in the $Pt/CoO_x/Al_2O_3$-600 H_2-aged sample remained nearly unchanged, decreasing slightly from 47.6% to 46.0%, indicating that Pt^0 remained relatively stable during high-temperature treatment. The observed stability of Pt^0 at relatively high temperatures can be attributed to the anchoring effect of the CoO_x support that inhibited further oxidation. In contrast, the Pt^{4+} content increased significantly from 27.51% to 45.46%, showing that a substantial portion of Pt^{2+} was oxidized under high-temperature oxidative conditions.

Journal Pre-proofs

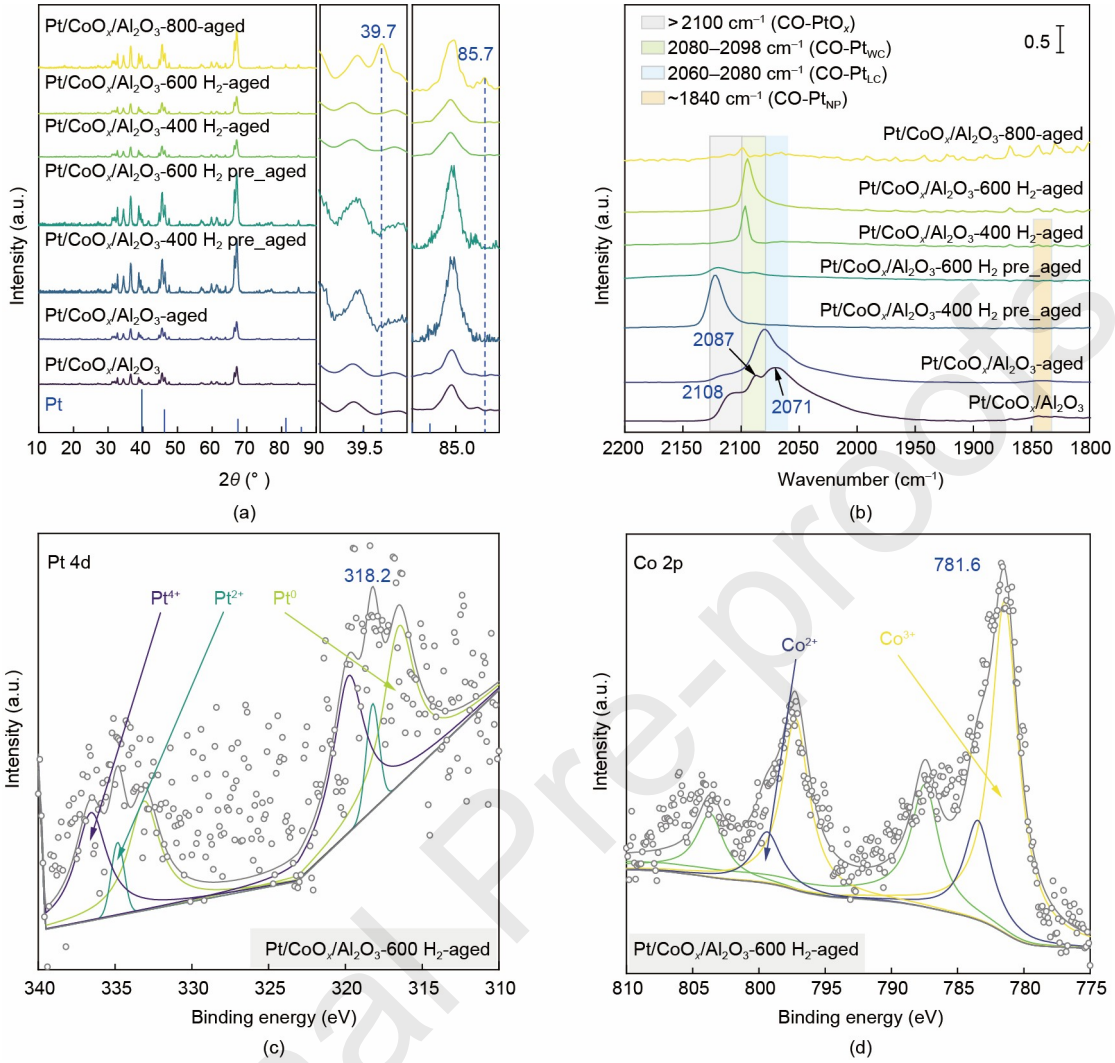

Fig. 4. (a) XRD patterns and (b) CO DRIFTS spectra of the pre- and post-treated Pt/CoO_x/Al_2O_3 samples after aging; XPS spectra of the Pt/CoO_x/Al_2O_3-600 H_2-aged sample: (c) Pt 4d orbital and (d) Co 2p orbital.

MD simulations were conducted to model the migration of CoO_x and Pt clusters on Al_2O_3. An MLP function capable of describing atomic interactions in the Al_2O_3-Co_3O_4-Pt system was constructed using the DeePMD framework. The procedure involves constructing the coordinate matrix $\boldsymbol{R}_{ij}$, converting it to an environment matrix $\boldsymbol{S}_{ij}$ using a custom smoothing function $s(r_{ij})$, and then processing it via a deep neural network. This procedure ensures invariance to translation, rotation, and permutation, effectively reflect the local chemical environment of the atom.

$$E = \sum_i N_{\alpha_i} \left(D_{\alpha_i} \left(r_i, \{r_j\} j \in n(i) \right) \right) \tag{2}$$

The descriptor $D_{\alpha_i}\left(r_i, \{r_j\} j \in n(i)\right)$ is constructed by integrating the information from a central atom i (with coordinates r_i) and its neighboring atoms $n(i)$ (with coordinates $\{r_j\}\, j \in n(i)$). E is the potential energy. For a system containing N atoms, the total potential energy E_{total} can be expressed as the sum of the local potential energy E_i of each atom: $E_{\text{total}} = E = \sum_i N_{\alpha_i}$.

To train a neural network, DeePMD uses a large amount of ab initio MD data, which include atomic coordinates, potential energy, and atomic forces under different atomic configurations. The mean squared error serves as the loss function L for both potential energy E and force F:

$$L_{\mathrm{E}} = \frac{1}{N_{\mathrm{samples}}} \sum_{k=1}^{N_{\mathrm{samples}}} \left(E_{\mathrm{pred}}^{k} - E_{\mathrm{true}}^{k} \right)^2 \tag{3}$$

$$L_{\mathrm{F}} = \frac{1}{N_{\mathrm{samples}}} \sum_{k=1}^{N_{\mathrm{samples}}} \frac{1}{N_{k=1}^{N_{\mathrm{atoms}}^{k}}} \sum_{i=1}^{N_{\mathrm{atoms}}^{k}} \left(F_{\mathrm{pred}}^{k,i} - F_{\mathrm{true}}^{k,i} \right)^2 \tag{4}$$

where N_{samples} represents the number of training samples; E_{pred}^{k} and E_{true}^{k} represent the predicted potential and true potential of the kth sample, respectively; N_{atoms}^{k} represents the number of atoms in the kth sample; $F_{\mathrm{pred}}^{k,i}$ and $F_{\mathrm{true}}^{k,i}$ represent the predicted and true forces on the ith atom in the kth sample, respectively.

The total loss function L_{total} is the weighted sum of the potential energy and force losses and is written as follows:

$$L_{\mathrm{total}} = \omega_E L_E + \omega_F L_F \tag{5}$$

where ω_E and ω_F are the weight coefficients used to balance the errors in potential energy and force, respectively. Using backpropagation algorithm, the network weights and biases were iteratively adjusted to minimize L_{total}. After training, the loss in potential energy was 8.36×10^{-3} and the loss in force was 6.39×10^{-2}, demonstrating that a highly accurate MLP was successfully obtained.

Fig. 5(a) and Fig. S12 in Appendix A present MD simulation results of high-temperature sintering of Pt clusters in the Pt/Al_2O_3 sample. Phases A–D illustrate the sequential stages of Pt cluster migration from 0 to 240 ps: initial state (A), onset (B), progression (C), and completion (D). Owing to the weak MSI between Pt and Al_2O_3, sintering was primarily governed by particle migration and coalescence, ultimately leading to migration and aggregation of Pt clusters into larger particles. Figs. 5(b)–(e) show the HAADF-STEM images, corresponding EDS mapping, and TEM image of the Pt/Al_2O_3-aged sample. The Pt clusters, highlighted by yellow circles, were clearly observed, with their distribution confirmed by EDS elemental mapping. Lattice fringes with a spacing of 0.22 nm, corresponding to the Pt (111) crystal facet, were visible in the bright-field images. These results demonstrate that the Pt clusters supported on Al_2O_3 exhibit poor thermal stability under high-temperature oxidative conditions. Fig. S13 in Appendix A further supports these findings, showing bright- and dark-field TEM images of the Pt/Al_2O_3-aged sample, showing enlarged Pt particles and, in turn, confirming significant sintering. Figs. S14–S16 in Appendix A present MD simulation and TEM characterization results of the Pt/CoO_x-aged samples. Owing to the enhanced MSI, sintering of the Pt clusters in the Pt/CoO_x system during high-temperature treatment was primarily governed by Ostwald ripening, with Pt clusters migrating and aggregating, ultimately leading to growth of the larger clusters at the expense of smaller ones. The stronger anchoring effect of CoO_x on the Pt clusters limited the extent of sintering compared with that in the Pt/Al_2O_3 system. However, lattice fringe with a spacing of 0.22 nm, corresponding to the Pt (111) facet, were still observed in relatively large Pt particles.

Fig. 5(f) and Fig. S17 in Appendix A present the adsorption structure constructed on the Al_2O_3 (001) surface using Materials Studio (BIOVIA, USA), along with MD simulations of Pt sintering on CoO_x and Al_2O_3. The introduction of CoO_x nano-islands significantly suppressed the sintering Pt clusters. Owing to the inherently high surface areas of the powder supports, achieving 100% ASD of Pt clusters exclusively on the Co_3O_4 was challenging. A small fraction of Pt clusters may have been deposited on the Al_2O_3 surface during the synthesis of the Pt/CoO_x/Al_2O_3 sample. Notably, the Pt clusters were significantly affected by the difference in MSI during subsequent thermal treatment. Specifically, the MSI between Pt and Al_2O_3 is relatively weak, facilitating sintering via the PMC mechanism. In contrast, the stronger MSI between Pt and Co_3O_4 helped stabilize the Pt clusters. Therefore, the Pt clusters initially located on Al_2O_3 tended to migrate toward CoO_x on the surface, where they became more effectively anchored through the enhanced MSI provided by CoO_x. The simulations suggest that Pt clusters on Al_2O_3 preferentially migrate toward CoO_x, especially at the interfaces where strong and weak MSI coexist. A certain degree of CoO_x aggregation is also observed, consistent with the experimental results. Figs. 5(g)–(j) show TEM and EDS maps of the Pt/CoO_x/Al_2O_3-600 H_2-aged

sample. The EDS results show that the solid pink contour in Fig. 5(g) corresponds to CoO_x clusters rather than to newly formed Pt particles, confirming the structural stability of Pt within the designed configuration. This stability of the system can be attributed to the combined effects of physical isolation by CoO_x nano-islands and the anchoring strength provided by MSI.

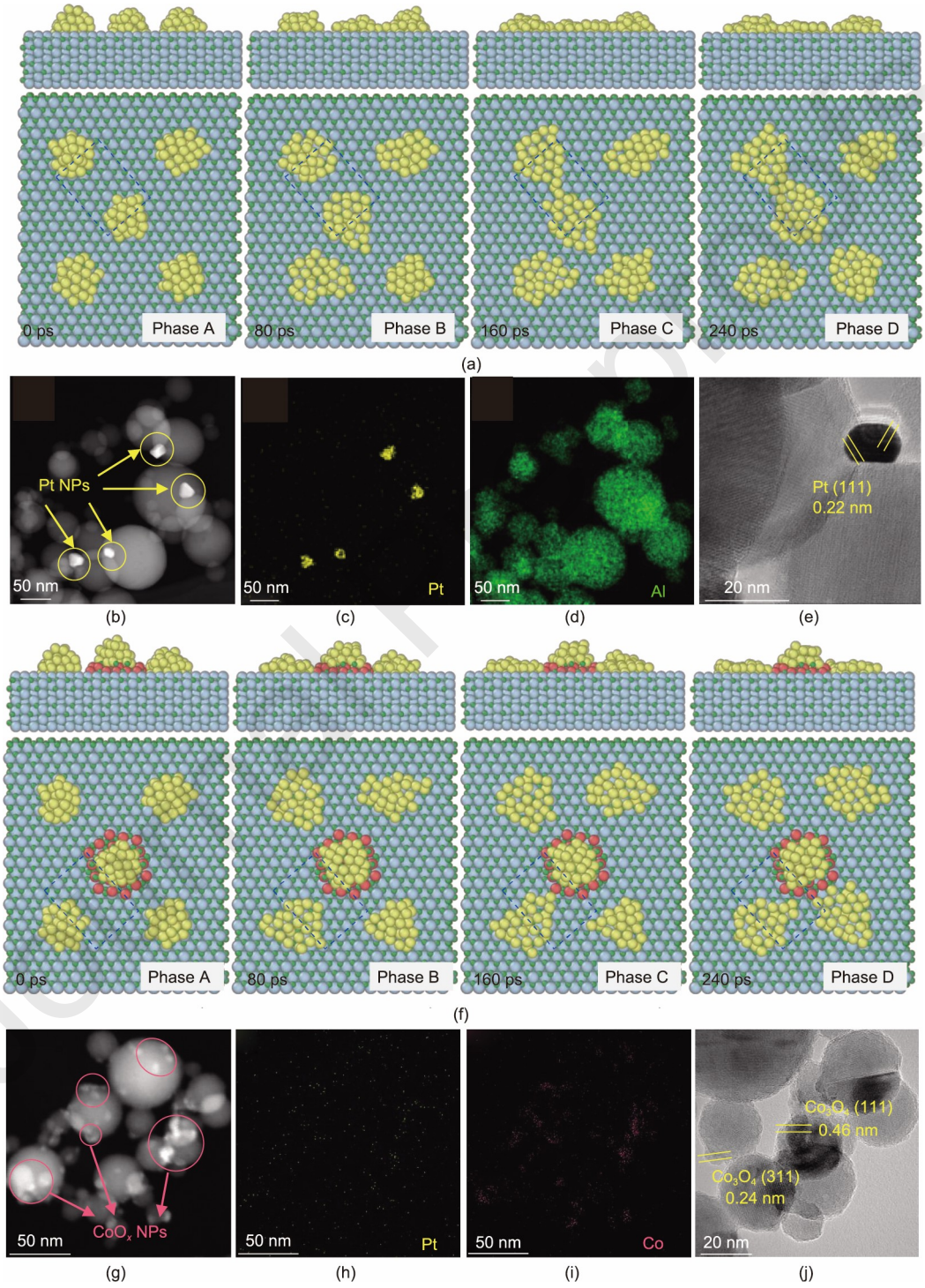

Fig. 5. (a) MD simulation results of the sintering process of Pt clusters in Pt/Al_2O_3, in which green, blue, and yellow spheres represent O, Al, and Pt atoms, respectively; characterization results obtained on the Pt/Al_2O_3-aged sample: (b–d) HAADF-STEM images and corresponding EDS mapping; (e) TEM image; (f) MD simulation results of the sintering process of Pt clusters in $Pt/CoO_x/Al_2O_3$, in which red, green, blue, and yellow spheres represent Co, O, Al, and Pt atoms, respectively; the results of $Pt/CoO_x/Al_2O_3$-600 H_2 aged sample: (g–i) HAADF-STEM and EDS mapping; and (j) TEM image.

5. Conclusions

A robust strategy has been demonstrated for enhancing the thermal stability of sub-nanometer metal clusters through precise structural design and interfacial engineering. By employing ASD, sub-nanometer Pt clusters (~0.76 nm) were spatially confined to CoO_x domains, achieving a high selectivity driven by intrinsic differences in precursor–surface interactions. The deposition process was optimized to achieve a high selectivity of 95.1%, and subsequent H_2 treatment further strengthened the MSI, promoting the thermodynamically favorable migration of Pt clusters toward the energetically favored CoO_x–Al_2O_3 interface regions. The synergistic interplay between spatial confinement and interfacial anchoring effectively suppressed sintering during both oxidative and reductive treatment at 600 °C, as confirmed by both atomistic simulations and experimental characterizations. These findings establish a generalized framework for designing thermally durable nanomaterials and provide valuable guidance for advancing energy systems, environmental remediation, and high-temperature structural materials.

Acknowledgments

This work is supported by the National Natural Science Foundation of China (52273237, 92580206 and 52350349), and the New Cornerstone Science Foundation through the XPLORER PRIZE. The authors would also like to acknowledge the technical support from the Analytic Testing Center and the Flexible Electronics Research Center of the Huazhong University of Science and Technology.

References

[1] Zhou T, Li X, Zhao J, Luo L, Wang Y, Xiao Z, et al. Ultrafine metal nanoparticles isolated on oxide nano-islands as exceptional sintering-resistant catalysts. Nat Mater 2025;24(6):891–9.

[2] Min J, Seo H, Shin J, Park MY, Park SY, Choi H, et al. Atomically dispersed platinum electrocatalysts supported on gadolinia-doped ceria nanoparticles for practical high-temperature solid oxide cells. J Mater Chem A 2023;11(46):25298–307.

[3] Gao Y, Li Q, Wang C, Yan D, Chen J, Jia H. Light-driven efficient dry reforming of methane over Pt/La_2O_3 with long-term durability. J Mater Chem A 2022;10(30):16016–28.

[4] Liang L, Jin H, Zhou H, Liu B, Hu C, Chen D, et al. Cobalt single atom site isolated Pt nanoparticles for efficient ORR and HER in acid media. Nano Energy 2021;88:106221.

[5] Ren Y, Chen K, Zhang Y, Shi D, Wu Q, Liang D, et al. N-doped carbon confined CoFe@Pt nanoparticles with robust catalytic performance for the methanol oxidation reaction. J Mater Chem A Mater Energy Sustain 2022;10(25):13345–54.

[6] Campbell CT, Mao Z. Chemical potential of metal atoms in supported nanoparticles: dependence upon particle size and support. ACS Catal 2017;7(12):8460–6.

[7] Xiao Y, Zhang J, Liu T, Xu M, Dong Y, Wang CA. Constructing morphologically stable supported noble metal catalysts in heterogeneous catalysis: mechanisms and strategies. Nano Energy 2024;129(Pt A):109975.

[8] Hu S, Li W. Influence of particle size distribution on lifetime and thermal stability of ostwald ripening of supported particles. ChemCatChem 2018;10(13):2900–7.

[9] Sarnello E, Lu Z, Seifert S, Winans RE, Li T. Design and characterization of ALD-based overcoats for supported metal nanoparticle catalysts. ACS Catal 2021;11(5):2605–19.

Journal Pre-proofs

[10] Solano E, Dendooven J, Feng JY, Brüner P, Minjauw MM, Ramachandran RK, et al. *In situ* study of the thermal stability of supported Pt nanoparticles and their stabilization via atomic layer deposition overcoating. Nanoscale 2020;12(21):11684–93.

[11] Cargnello M, Delgado Jaén JJ, Hernández Garrido JC, Bakhmutsky K, Montini T, Calvino Gámez JJ, et al. Exceptional activity for methane combustion over modular Pd@CeO_2 subunits on functionalized Al_2O_3. Science 2012;337(6095):713–7.

[12] Adijanto L, Bennett DA, Chen C, Yu AS, Cargnello M, Fornasiero P, et al. Exceptional thermal stability of Pd@CeO_2 core-shell catalyst nanostructures grafted onto an oxide surface. Nano Lett 2013;13(5):2252–7.

[13] Cao A, Veser G. Exceptional high-temperature stability through distillation-like self-stabilization in bimetallic nanoparticles. Nat Mater 2010;9(1):75–81.

[14] Carrillo C, DeLaRiva A, Xiong H, Peterson EJ, Spilde MN, Kunwar D, et al. Regenerative trapping: how Pd improves the durability of Pt diesel oxidation catalysts. Appl Catal B 2017;218:581–90.

[15] Chen R, Li YC, Cai JM, Cao K, Lee HBR. Atomic level deposition to extend Moore's law and beyond. Int J Extreme Manuf 2020;2(2):022002.

[16] Chen R, Gu E, Cao K, Zhang J. Area selective deposition for bottom-up atomic-scale manufacturing. Int J Mach Tools Manuf 2024;199:104173.

[17] Chen R, Cao K, Wen Y, Yang F, Wang J, Liu X, et al. Atomic layer deposition in advanced display technologies: from photoluminescence to encapsulation. Int J Extreme Manuf 2024;6(2):022003.

[18] Li Y, Qi Z, Lan Y, Cao K, Wen Y, Zhang J, et al. Self-aligned patterning of tantalum oxide on Cu/SiO_2 through redox-coupled inherently selective atomic layer deposition. Nat Commun 2023;14(1):4493.

[19] Cheng N, Banis MN, Liu J, Riese A, Li X, Li R, et al. Extremely stable platinum nanoparticles encapsulated in a zirconia nanocage by area-selective atomic layer deposition for the oxygen reduction reaction. Adv Mater 2015;27(2):277–81.

[20] Aitbekova A, Zhou C, Stone ML, Lezama-Pacheco JS, Yang AC, Hoffman AS, et al. Templated encapsulation of platinum-based catalysts promotes high-temperature stability to 1,100 °C. Nat Mater 2022;21(11):1290–7.

[21] Cao K, Shi L, Gong M, Cai J, Liu X, Chu S, et al. Nanofence stabilized platinum nanoparticles catalyst via facet-selective atomic layer deposition. Small 2017;13(32):1700648.

[22] Liu X, Zhu Q, Lang Y, Cao K, Chu S, Shan B, et al. Oxide-nanotrap-anchored platinum nanoparticles with high activity and sintering resistance by area-selective atomic layer deposition. Angew Chem Int Ed Engl 2017;56(6):1648–52.

[23] Li X, Pereira-Hernández XI, Chen Y, Xu J, Zhao J, Pao CW, et al. Functional CeO_x nanoglues for robust atomically dispersed catalysts. Nature 2022;611(7935):284–8.

[24] Hu S, Li WX. Sabatier principle of metal-support interaction for design of ultrastable metal nanocatalysts. Science 2021;374(6573):1360–5.

[25] Jones J, Xiong H, DeLaRiva AT, Peterson EJ, Pham H, Challa SR, et al. Thermally stable single-atom platinum-on-ceria catalysts via atom trapping. Science 2016;353(6295):150–4.

[26] Li Z, Li B, Li Q. Single-atom nano-islands (SANIs): a robust atomic-nano system for versatile heterogeneous catalysis applications. Adv Mater 2023;35(20):2211103.

[27] Liu JC, Luo L, Xiao H, Zhu J, He Y, Li J. Metal affinity of support dictates sintering of gold catalysts. J Am Chem Soc 2022;144(45):20601–9.

[28] Cai J, Liu Z, Cao K, Lang Y, Chu S, Shan B, et al. Highly dispersed Pt studded on CoO_x nanoclusters for CO preferential oxidation in H_2. J Mater Chem 2020;8(20):10180–7.

[29] Bobb-Semple D, Nardi KL, Draeger N, Hausmann DM, Bent SF. Area-selective atomic layer deposition assisted by self-assembled monolayers: a comparison of Cu, Co, W, and Ru. Chem Mater 2019;31(5):1635–45.

[30] Gladfelter WL. Selective metalization by chemical vapor deposition. Chem Mater 1993;5(10):1372–88.

Journal Pre-proofs

[31] Yu X, Yu W, Li H, Tu ST, Han YF. Preparation, characterization and application of K-PtCo/Al_2O_3 catalyst coatings for preferential CO oxidation. Appl Catal B 2013;140–141:588–97.

[32] Choya A, de Rivas B, Gutiérrez-Ortiz JI, López-Fonseca R. Comparative study of strategies for enhancing the performance of Co_3O_4/Al_2O_3 catalysts for lean methane combustion. Catalysts 2020;10(7):757.

[33] Dong Y, He K, Yin L, Zhang A. A facile route to controlled synthesis of Co_3O_4 nanoparticles and their environmental catalytic properties. Nanotechnology 2007;18(43):435602.

[34] Zhao R, Cao K, Ye R, Tang Y, Du C, Liu F, et al. Deciphering the stability mechanism of Pt-Ni/Al_2O_3 catalysts in syngas production via DRM. Chem Eng J 2024;491:151966.

[35] Xiong G, Feng C, Chen HC, Li J, Jiang F, Tao S, et al. Atomically dispersed Pt-doped Co_3O_4 spinel nanoparticles embedded in polyhedron frames for robust propane oxidation at low temperature. Small Methods 2023;7(7):2300121.

[36] Lin J, Zhao S, Yang J, Huang W, Chen C, Chen T, et al. Hydrogen spillover induced PtCo/CoO_x interfaces with enhanced catalytic activity for CO oxidation at low temperatures in humid conditions. Small 2024;20(22):2309181.

[37] Raskó J. CO-induced surface structural changes of Pt on oxide-supported Pt catalysts studied by DRIFTS. J Catal 2003;217(2):478–86.

[38] Macino M, Barnes AJ, Althahban SM, Qu R, Gibson EK, Morgan DJ, et al. Tuning of catalytic sites in Pt/TiO_2 catalysts for the chemoselective hydrogenation of 3-nitrostyrene. Nat Catal 2019;2(10):873–81.

[39] Pham HN, DeLaRiva A, Peterson EJ, Alcala R, Khivantsev K, Szanyi J, et al. Designing ceria/alumina for efficient trapping of Platinum single atoms. ACS Sustain Chem Eng 2022;10(23):7603–12.

[40] Han B, Guo Y, Huang Y, Xi W, Xu J, Luo J, et al. Strong metal-support interactions between Pt single atoms and TiO_2. Angew Chem Int Ed Engl 2020;59(29):11824–9.

[41] Lee HBR, Pickrahn KL, Bent SF. Effect of O_3 on growth of Pt by atomic layer deposition. J Phys Chem C 2014;118(23):12325–32.

[42] Erkens IJM, Mackus AJM, Knoops HCM, Smits P, van de Ven THM, Roozeboom F, et al. Mass spectrometry study of the temperature dependence of Pt film growth by atomic layer deposition. ECS J Solid State Sci Technol 2012;1(6):P255.

[43] Baker L, Cavanagh AS, Seghete D, George SM, Mackus AJM, Kessels WMM, et al. Nucleation and growth of Pt atomic layer deposition on Al_2O_3 substrates using (methylcyclopentadienyl)-trimethyl platinum and O_2 plasma. J Appl Phys 2011;109(8):084333.

[44] Knoops HCM, Mackus AJM, Donders ME, van de Sanden MCM, Notten PHL, Kessels WMM. Remote plasma ALD of platinum and platinum oxide films. Electrochem Solid-State Lett 2009;12(7):G34.

[45] Knoops HC, Mackus A, Donders M, Van de Sanden MC, Notten P, Kessels WM. Remote plasma and thermal ALD of platinum and platinum oxide films. ECS Trans 2008;16(4):209.

[46] Wang W, Chen X, Cai Q, Mo G, Jiang LS, Zhang K, et al. *In situ* SAXS study on size changes of platinum nanoparticles with temperature. Eur Phys J B 2008;65(1):57–64.

[47] Dinh KHT, Ta HTT, Nguyen NL, Le VT, Nguyen VH, Van Bui H. Dimension control of Platinum nanostructures by atomic layer deposition: from surface chemical reactions to applications. Chem Mater 2023;35(6):2248–80.

[48] Lentz C, Jand SP, Melke J, Roth C, Kaghazchi P. DRIFTS study of CO adsorption on Pt nanoparticles supported by DFT calculations. J Mol Catal A 2017;426(Part A):1–9.

[49] Wang Y, Zhu B, Cheng B, Macyk W, Kuang P, Yu J. Hollow carbon sphere-supported Pt/CoO_x hybrid with excellent hydrogen evolution activity and stability in acidic environment. Appl Catal B 2022;314:121503.

Compliance with ethics guidelines

All authors (the name of author) declare that they have no conflict of interest or financial conflicts to disclose.

Journal Pre-proofs